

<https://doi.org/10.1038/s42005-024-01753-z>

Tilted stripes origin in $\text{La}_{1.88}\text{Sr}_{0.12}\text{CuO}_4$ revealed by anisotropic next-nearest neighbor hopping

Check for updates

Wei He^{1,2,7}✉, Jiajia Wen¹, Hong-Chen Jiang¹, Guangyong Xu³, Wei Tian⁴, Takatori Taniguchi⁵, Yoichi Ikeda⁵, Masaki Fujita⁵ & Young S. Lee^{1,6}✉

Spin- and charge- stripe order has been extensively studied in the superconducting cuprates, among which underdoped $\text{La}_{2-x}\text{Sr}_x\text{CuO}_4$ (LSCO) is an archetype with static spin stripes at low temperatures. An intriguing, but not completely understood, phenomenon in LSCO is that the stripes are tilted away from the high-symmetry Cu-Cu directions. Using high-resolution neutron scattering on LSCO with $x = 0.12$, we find two coexisting phases at low temperatures, one with static spin stripes and the other with fluctuating ones, both sharing the same tilt angle. Our numerical calculations using the doped Hubbard model elucidate the tilting's origin, attributing it to anisotropic next-nearest neighbor hopping t' , consistent with the material's slight orthorhombicity. Our results underscore the model's success in describing specific details of the ground state of this real material and highlight the role of t' in the Hamiltonian, revealing the delicate interplay between stripes and superconductivity across theoretical and experimental contexts.

The high- T_c cuprates exhibit complex physical phenomena due to the presence of various phases which may interact with the superconductivity¹. In recent years, the existence of charge density wave (CDW) and spin density wave (SDW) order has been observed across many families of cuprates^{2,3}. The La-based family is a canonical example where both the spin and charge orders form “stripes” which are especially stable near 1/8 hole doping^{4–6}. In the stripe model, the doped holes segregate into unidirectional stripes which serve as the antiphase domain boundaries between patches of antiferromagnetically correlated spins. Since the periodicity of the spin order is twice that of the charge order, the wave vectors of these two orders satisfy the relationship $\delta_{\text{charge}} = 2\delta_{\text{spin}}$, which has been confirmed by extensive neutron and x-ray scattering measurements^{5,6}.

A phenomenon that is not completely understood is that the direction of the stripes is slightly tilted from the underlying Cu-Cu direction. This follows from the observations of small in-plane shifts of both the SDW and CDW peak positions from the high-symmetry directions in orthorhombic cuprates^{7–16}. This observation was referred to as the *Y*-shift in early measurements⁸, and we will use this term to refer to the observation that denotes tilted stripes. Specifically, in $\text{La}_{2-x}\text{Sr}_x\text{CuO}_4$ (LSCO), the CuO_2 square lattice is deformed upon cooling from a high-temperature tetragonal

to a low-temperature orthorhombic structure. As sketched in Fig. 1a, the average tilting of the charge domain wall boundaries has a specific orientation with the orthorhombic distortion. This phenomenon was first discovered in oxygen-doped $\text{La}_2\text{CuO}_{4+y}$ (LCO)⁷ and subsequently observed in other systems, including LSCO^{8,9,13} and $\text{La}_{1.875}\text{Ba}_{0.125-x}\text{Sr}_x\text{CuO}_4$ ¹⁰. Recent x-ray scattering of the CDW order in LSCO^{11,15,16} also confirmed the existence of the *Y*-shift in the charge stripes, consistent with the SDW order, further corroborating the stripe picture. Such a shift is expected in the phenomenological Landau-Ginzburg model for incommensurate stripe orders in the presence of an orthorhombic distortion¹⁷. However, the microscopic origin of the *Y*-shift was still not clear.

Recently, new insights regarding the stripe phases and superconductivity have come from numerical simulations using the doped Hubbard model (and *t*-*J* model) to describe the CuO_2 planes. Half-filled stripes, which are consistent with the periodicities observed for doped LSCO, are found using interaction terms U , t , and t' ^{18–25}, where U is the on-site Coulomb repulsion and t (t') is the (next) nearest neighbor hopping. The significance of t' in the cuprates is strongly suggested by the observation that filled stripes (with double the periodicity, inconsistent with LSCO) are favored when only U and t are used in the model^{22,26}. Recent density-matrix

¹Stanford Institute for Materials and Energy Sciences, SLAC National Accelerator Laboratory, Menlo Park, CA, 94025, USA. ²Department of Materials Science and Engineering, Stanford University, Stanford, CA, 94305, USA. ³NIST Center for Neutron Research, National Institute of Standards and Technology, Gaithersburg, MD, 20899-6102, USA. ⁴Neutron Scattering Division, Oak Ridge National Laboratory, Oak Ridge, TN, 37831, USA. ⁵Institute for Materials Research, Tohoku University, Sendai, 980-8577, Japan. ⁶Department of Applied Physics, Stanford University, Stanford, CA, 94305, USA. ⁷Present address: Department of Condensed Matter Physics and Materials Science, Brookhaven National Laboratory, Upton, NY, 11973, USA. ✉e-mail: weh1@bnl.gov; youngsl@stanford.edu

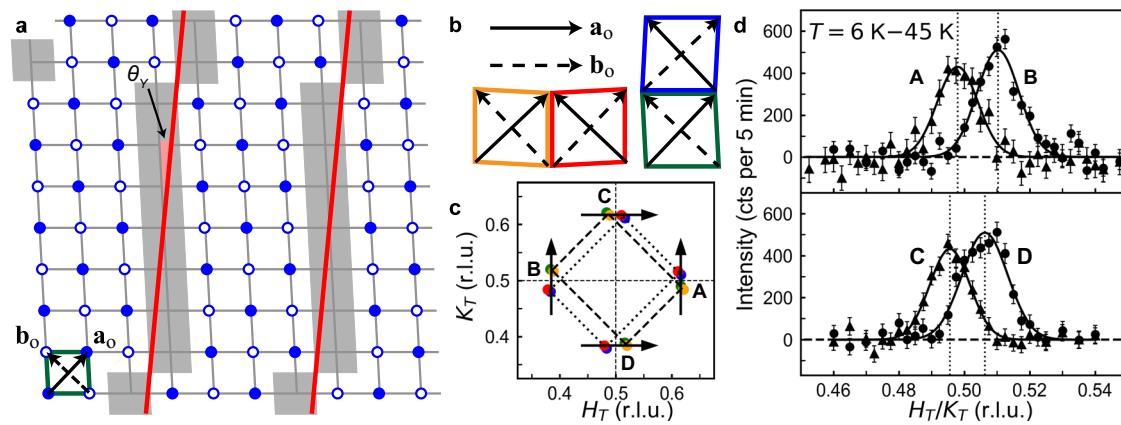


Fig. 1 | Tilted stripes and the crystal structure. **a** A schematic of the CuO₂ plane with orthorhombic distortion and the tilted spin- and charge- stripe order. Solid and open blue circles denote spins with opposite directions. The solid green lines show the tetragonal unit cell. The gray regions are the charge stripes served as antiphase domain walls for the magnetic stripes and the red lines show the tilted average stripe direction. **b** Tetragonal unit cells of the four structural twin domains in the orthorhombic phase. **c** Corresponding possible SDW peaks around (0.5, 0.5, 0) in reciprocal space. The two rectangles formed by the two sets of peaks (red and blue vs.

green and orange) have different centers due to orthorhombic distortion. The solid (dashed) arrows in (a, b) show the orthorhombic a_0 (b_0) direction. The orthorhombic distortion and Y -shift in a–c are exaggerated for clarity. **d** Elastic neutron scattering of the SDW peaks at 6 K with the 45 K data subtracted as a background. The solid lines are Gaussian fits to the data. The vertical dotted lines are the fitted peak centers. The trajectory of each scan is denoted in c. Error bars correspond to $\pm\sigma$, where σ is the standard deviation.

renormalization group (DMRG) calculations have shown that the presence of t' is also necessary to induce superconducting correlations^{21–23}. Here, we use DMRG simulations to determine the terms in the Hubbard model that can stabilize the tilted stripes in LSCO with $x = 0.12$. We find that t' plays a crucial role, and that the tilted alignment of stripes is highly sensitive to small anisotropies in t' , quantitatively consistent with the experimental results.

Another issue to address is whether the tilting phenomenon is particular to static stripes, or if it is generic to the stripe correlations which may also be fluctuating. Spin fluctuations are ubiquitous in the phase diagram of cuprates². In the stripe picture, the low-energy spin fluctuations may be thought of as spin waves associated with the ordered stripes, i.e., dynamic stripes^{27–30}, but the universality of this description is still under debate³¹. Due to the broad widths and weak cross sections of the spin fluctuation peaks, it is extremely challenging to detect small peak shifts in the inelastic neutron scattering. Most of the previous studies of the Y -shift focused on static stripes, and it remains an open question whether the static and fluctuating spin correlations are characterized by the same stripe tilting.

Here, we present our comprehensive high-resolution neutron scattering study of the Y -shift phenomenon on a single crystal of LSCO with $x = 0.12$, which has the longest length scale for the spin correlations³². The sample was mounted in the $(HK0)$ zone, and tetragonal notation is used unless otherwise noted. More details of the experiments can be found in the Methods. First, our elastic scattering results verify the existence of the Y -shift in static SDW order. To the best of our knowledge, we determine the spin direction in LSCO for the first time, and provide a new method to determine the interlayer correlations. Then, the inelastic scattering results offer evidence for the same Y -shift in the dynamic spin stripes, where the spin fluctuation direction is found to be predominantly isotropic. Finally, our numerical calculations using the DMRG method³³ explain the microscopic origin of the Y -shift. The anisotropy of the next-nearest neighbor hopping term t' plays a key role here.

Results

Tilted static spin stripes

To begin, a proper interpretation of the neutron scattering data requires a careful understanding of the structural twinning in our LSCO single crystal sample. As depicted in Fig. 1b, the orthorhombic distortion leads to four possible structural twin domains³⁴. From the precise characterization of nuclear Bragg peaks (see Supplementary Note 1, Supplementary Fig. 1, and Supplementary Tab. 1), we find that our sample has all four domains with

similar populations and the orthorhombicity is $0.38(2)^\circ$ (calculated as $\frac{b_0 - a_0}{a_0}$, where a_0 and b_0 are in-plane lattice parameters in orthorhombic notation).

We start with the elastic magnetic scattering of the SDW order near the antiferromagnetic zone center of (0.5, 0.5, 0). A quartet of SDW peaks can be observed here due to the existence of two magnetic domains (different from the structural twin domains above) with stripe directions perpendicular to each other. Figure 1d shows representative scans along the tetragonal H or K directions. The two magnetic domains have roughly the same populations, indicated by the similar intensities between the two pairs of peaks (e.g., peak A vs. C, or peak B vs. D). Within each pair of peaks, a clear shift is observed, corresponding to a Y -shift angle of $3.0(2)^\circ$, consistent with previous reports⁸. However, a mystery observation is the presence of only a single peak in each scan, in contrast to the predicted pattern in Fig. 1c based on the existence of four equally-populated structural twin domains. Further inspection (see Supplementary Note 2) indicates that the observed peaks can only originate from the orange and green structural domains, both of which have the shorter orthorhombic a_0 axis nearly aligned with (0.5, 0.5, 0). The in-plane correlation length is determined to be $123(7)\text{ \AA}$ (see Supplementary Fig. 2 and Supplementary Tab. 2).

We propose two models to explain the missing contributions from the other two twin domains. As illustrated in Fig. 2a, the first model involves the coupling between layers and therefore is named the “3D stacking model”. The depicted stacking arrangement (which is locally similar to that in La₂CuO₄³⁵) results in nearly zero intensity around (0.5, 0.5, 0) for the red and blue domains. The second model depends on the spin direction, relying on the fact that the magnetic neutron scattering cross section is only sensitive to components of the spin \mathbf{S} that are perpendicular to the wavevector \mathbf{Q} . Hence, if the spins are pointing along the orthorhombic b_0 direction, as displayed in Fig. 2c, the red and blue domains will give nearly zero intensities around (0.5, 0.5, 0) regardless of the stacking arrangement between layers. Quantitatively, considering that the intensities from the red and blue domains around (0.5, 0.5, 0) are less than $\sim 5\%$ of those from the green and orange domains in Fig. 1d, the spins need to be either correlated over at least 14.3 \AA in the L direction using a finite-size domain analysis (see Supplementary Note 2D)³⁶ in the first model, or fixed to the orthorhombic b_0 direction within 10° in the second model.

Both spin models proposed above are reminiscent of the spin structure of the parent compound La₂CuO₄³⁵ and in oxygen-doped LCO⁷. To further distinguish the two models, one approach is to measure the L -dependence of the SDW intensity as in ref. 7. However, this method involves switching

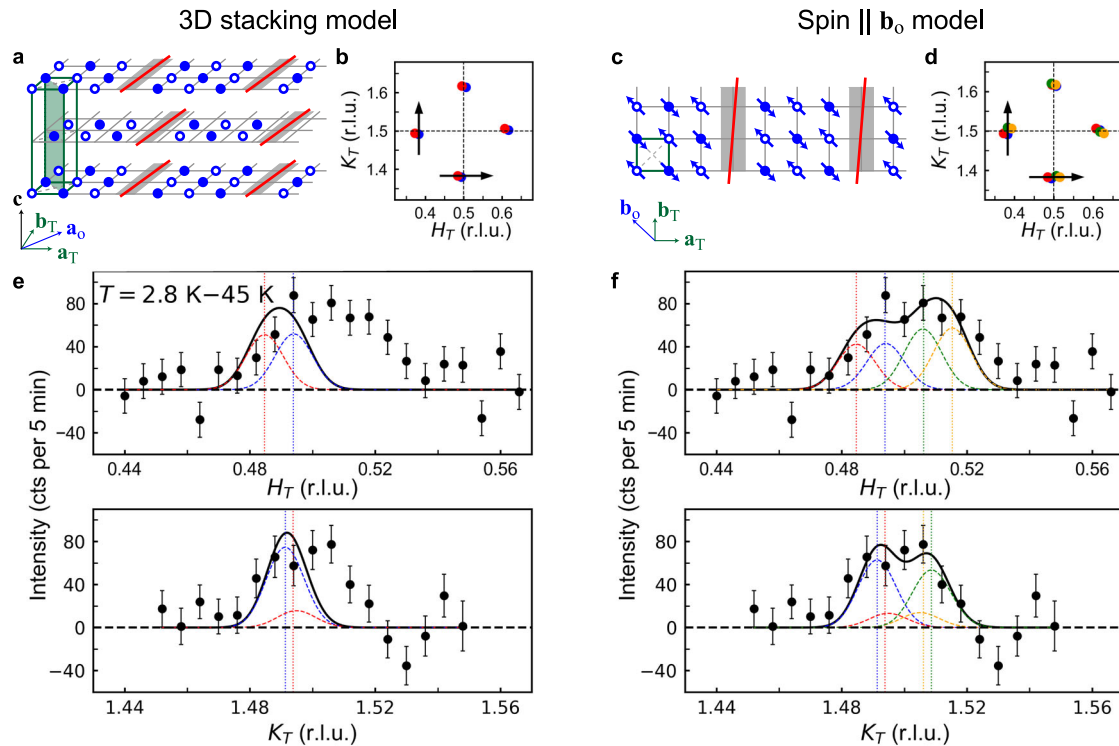


Fig. 2 | Comparison of two models for SDW peaks around (0.5, 1.5, 0). **a, b, e** are for the “3D stacking model” while **c, d** and **f** for the “Spin || b_0 model.” **a, c** show schematics of the two models in real space. The solid green lines denote the structural unit cell. The gray regions are the charge stripes and the red lines show the Y -shifted effective stripe direction. Solid and open blue circles denote spins with opposite directions. Arrows on top of the circles further specify spin directions in **c**. The spins in the neighboring layers have fixed relation in the 3D stacking model as shown in **a** while these long-range interlayer correlations are absent in the Spin || b_0 model.

b, d show the corresponding SDW peaks around (0.5, 1.5, 0) in reciprocal space. The colors of the peaks follow the convention in Fig. 1. **e, f** display elastic neutron scattering of these SDW peaks at 2.8 K with the 45 K data subtracted as a background. The solid black lines fit the data based on the two models with details in the text. The dashed curve shows the component from each peak with the center at the vertical dotted line. The trajectory of each scan is denoted in **b** and **d**. Error bars correspond to $\pm \sigma$, where σ is the standard deviation.

sample scattering geometry. As an alternate approach, we implement a strategy to distinguish these two models by going to higher Brillouin zones within the same ($HK0$) geometry. As shown in Fig. 2d near the (0.5, 1.5, 0) position, since the wavevector \mathbf{Q} no longer coincides with the spin directions, peaks from four domains should all contribute to the neutron scattering. However, if the 3D stacking model is correct, then peaks from the orange and green domains would be forbidden as drawn in Fig. 2b. Figure 2e demonstrates that the measured peak profiles clearly deviate from the expectations for the 3D stacking model. Therefore, the second model with spins aligned along the orthorhombic b_0 -axis should be preferred. Indeed, the fits based on this “spin || b_0 model” gives significantly improved agreement, as shown in Fig. 2f. Moreover, by co-fitting with the SDW peaks near (0.5, 0.5, 0), we can further quantify the interlayer correlation length and the volume fractions of stripe ordered phases (see Supplementary Note 2). Using a finite-size domain analysis³⁶, the interlayer correlation length is determined to be $7(1) \text{ \AA}$, corresponding to a slight modulation of intensities by $(20 \pm 15)\%$ along L .

The intensities of the fits in Fig. 2f (colored lines) indicate the static SDW does not occur homogeneously throughout the sample. Rather, only a partial fraction of the sample contains static SDW, where the red and blue structural domains contain 2.9(6) times more of the static SDW phase volume fraction compared to the other two domains, as evidenced in Supplementary Fig. 3. By normalizing the SDW peak intensities with the nuclear Bragg peaks, the average ordered moment at 6 K is deduced to be at most $0.07(1)\mu_B$, close to the previous reported values in LSCO^{37,38} but only about half of that in oxygen-doped LCO⁷. Assuming a local moment value of $0.36\mu_B$ from a previous μ SR report³⁹, this suggests the magnetic volume fraction is less than $\sim 5\%$. This value is lower than the ordered fraction of 18% from the μ SR study³⁹, possibly due to sample variation and differing

sensitivities of the probes. μ SR is a more localized probe, whereas neutron scattering detects long-range ordered spins. The implications of the minority static SDW phase are further discussed in the Discussion Section.

Determination of tilting for the fluctuating spin stripes

Armed with the detailed knowledge learned from elastic neutron scattering (such as the structural domain population, magnetic structure, Y -shift angle in the static SDW phase, etc.), we next turn to high-resolution inelastic scattering to study the low-energy excitations of the spin stripes. Figure 3a–b shows scans around (0.5, 0.5, 0) at two representative energy transfers at 30 K, which is close to the onset temperature of the SDW order T_{sdw} ³⁷ and has the highest intensities (evidenced in Fig. 4b). The energy dependence of the inelastic peak shift is plotted in Fig. 3c. Although the shifts here are much smaller than the elastic case, their consistently non-zero values indicate that the dynamic stripes also have a Y -shift. Note that the case assuming no Y -shift for the inelastic scattering is given by the dotted line near zero shift (this value includes a very small correction taking into account the structural domain populations). Our data show that the fluctuating stripes are tilted with the same tilt angle of $\sim 3.0^\circ$ as observed for the static spin stripes. That is, our analysis indicates that the inelastic peaks appearing at the same positions as their elastic counterparts in the low-energy limit, consistent with the Goldstone theorem. Recent findings that the Y -shift exists in the CDW order at $\sim T_{sdw}$ in LSCO^{11,15,16} with the shift angle similar to low temperatures are consistent with this notion.

The reason that the apparent Y -shift is much smaller than that in the elastic scattering is simply an averaging effect of the structural twin domains. As seen in the analysis of the elastic magnetic cross section, the inelastic scattering intensities are also affected by the neutron polarization factor and interlayer correlations. Specifically, for the inelastic peaks around (0.5, 0.5, 0),

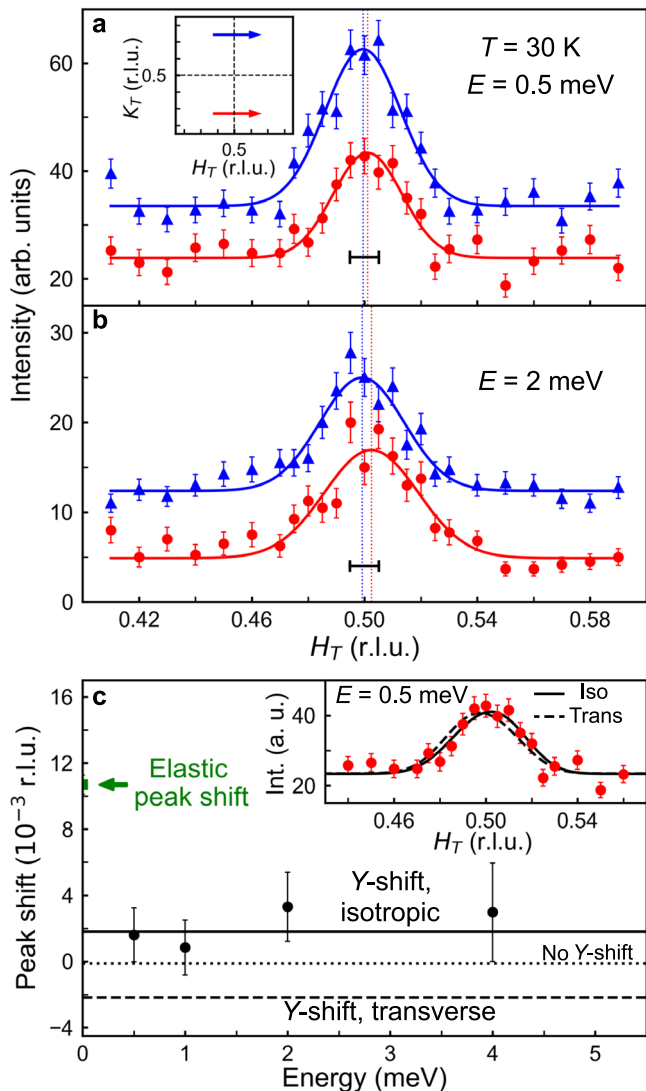


Fig. 3 | Energy dependence of the dynamic spin stripes. **a, b** Inelastic neutron scattering of the spin stripes at 30 K for an energy transfer of $E = 0.5$ meV (**a**) and $E = 2$ meV (**b**). The solid lines are Gaussian fits with a constant background and the vertical dotted lines are the fitted peak centers. The trajectory of each scan is denoted in the inset of **a**. The horizontal bars represent the elastic peak shift. The blue data are shifted vertically for clarity. **c** Energy dependence of the peak shift between the fitted centers of a pair of peaks as shown in **a, b** and Supplementary Fig. 5. Solid and dashed lines are the expected peak shift for isotropic and transverse spin fluctuations ΔS with Y-shift, respectively, while the dotted line for isotropic spin fluctuations without Y-shift. Inset: the same red data in **a** with fits assuming isotropic (solid line) and transverse (dashed line) excitations with Y-shift. Error bars correspond to $\pm\sigma$, where σ is the standard deviation.

the interlayer correlations reduce the intensities of the red and blue domains by $\sim 20\%$. The neutron polarization factor has a bigger effect, resulting in essentially zero intensities for the longitudinal spin fluctuations ΔS from the red and blue domains and essentially zero intensities for the in-plane transverse spin fluctuations of the orange and green domains. Here, longitudinal and transverse spin fluctuation directions are with respect to the static spin direction. With these constraints in mind, we calculate the weighted peak position for various cases.

We can first rule out the scenario in which the inelastic signal arises only from the magnetically ordered regions. In that case, the peaks have dominant contributions from the red and blue domains due to their larger stripe volume fraction and therefore shift to the opposite direction (see Supplementary Fig. 6). Hence, we can conclude that the inelastic scattering

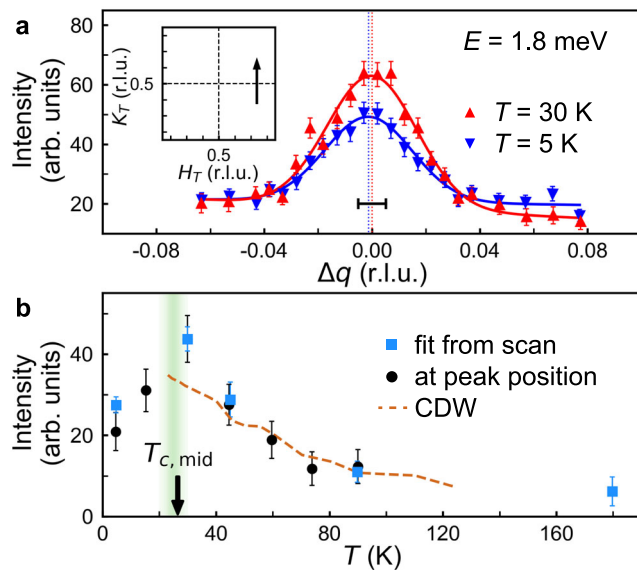


Fig. 4 | Temperature dependence of the dynamic spin stripes. **a** Representative scans at 5 K and 30 K for an energy transfer of $E = 1.8$ meV. The scan trajectory is shown in the inset. The solid lines are Gaussian fits with a linear background and the vertical dotted lines are the fitted peak centers. The horizontal bar represents the elastic peak shift. **b** Integrated intensity extracted from the Gaussian fits (blue squares). The black circles are intensities from one-point measurement at the peak position and scaled to match the fitted integrated intensity at 30 K. The arrow indicates the midpoint temperature (26.5 K) of the superconducting transition $T_{c, \text{mid}}$. The diffuse green vertical line indicates the SDW onset temperature varying from ~ 20 K (μSR^{39}) to ~ 30 K (neutron³⁹). The brown dashed line is the integrated intensity of CDW peak measured by resonant soft x-ray scattering¹⁵ and scaled to match our data. Error bars correspond to $\pm\sigma$, where σ is the standard deviation.

likely originates from the whole sample rather than just the magnetically ordered regions. Then we test two extreme cases: purely isotropic excitations and purely transverse excitations. As shown in Fig. 3c and Supplementary Fig. 8, the isotropic model clearly describes the data better. If we adopt this isotropic model, the fitted intrinsic tilt angle is $3.1(9)^\circ$, which, within the errors, is the same as that for the static spin stripes ($3.0(2)^\circ$). The observed small positive shift is primarily caused by the slight decrease of the intensities from the red and blue domains due to the finite interlayer correlations. The observed difference in the peak positions for the elastic and inelastic scattering is simply a domain-averaging effect, and phase separation explains the existence of the isotropic spin excitations (see further discussions in the Discussion Section).

We also investigate the temperature dependence of the inelastic scattering (see Fig. 4 and Supplementary Fig. 9). Even at 5 K, which is well below T_{sdw} , no obvious change of the peak position is observed relative to the 30 K data. Therefore, we can extend our previous conclusion of isotropic excitations to the low-temperature regime. This interpretation is consistent with recent results in oxygen-doped LCO⁴⁰. Another type of phase separation scenario has been suggested in LSCO emphasizing a dip in the excitation spectrum ~ 4 meV below T_c as a hidden-spin gap for the superconducting regions⁴¹. We do not observe a shift of the inelastic peak positions for energy transfers below 4 meV upon cooling, as shown in Fig. 4a. This could be due to a distribution of gap sizes and the energy we choose here (1.8 meV) is still above the spin gap in the majority of the sample. Energy-dependent measurements in the ordered state would be crucial to investigate this hidden-spin-gap hypothesis.

We also note that in Fig. 4b the intensities of spin fluctuations above T_{sdw} closely follow the trend of the CDW intensities recently measured using resonant soft x-ray scattering¹⁵. The extracted dynamical spin correlation length ($62(10)$ Å at $E = 0.5$ meV, see Supplementary Note 3 and Supplementary Fig. 7) is close to the CDW correlation length^{11,15,16}.

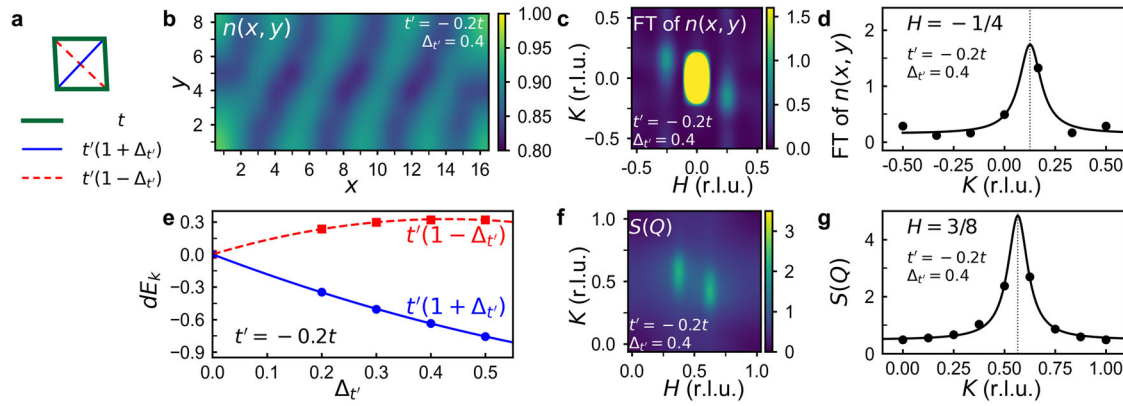


Fig. 5 | Numerical simulations of the origin of the stripe tilting. **a** The unit cell with orthorhombic distortion to illustrate the electron hopping terms used in the calculations. **b** The electron density distribution $n(x, y)$ calculated for $t' = -0.2t$ and $\Delta_{t'} = 0.4$. **c** The Fourier transform of the electron density distribution in **b**. **d** K -cut of the charge ordering peaks at $H = -0.25$ in **c**. **e** The kinetic energy differences as defined in the main text for $t' = -0.2t$. The lines are quadratic fits to the data. **f** The static spin structure factor $S(\mathbf{Q})$ calculated for $t' = -0.2t$ and $\Delta_{t'} = 0.4$. **g** K -cut of

the spin ordering peaks in $S(\mathbf{Q})$ at $H = 0.375$. The maps in **b**, **c**, **f** are produced using multiquadric interpolation method⁶⁹. The solid lines in **d**, **g** are Lorentzian fits with a constant background to determine the peak center (denoted by the vertical dotted lines). The Lorentzian peak widths for charge ordering and spin ordering peaks in the fitting are fixed to the best overall value based on data with all different $\Delta_{t'}$, respectively.

Numerical calculations: understanding the origin of the tilting

The experimental observation that the same tilting arrangement is inherent to both static and dynamic stripes calls for a microscopic explanation. Here, we study the spatially anisotropic t - t' Hubbard model on the square lattice using the DMRG method³³, which is defined by the Hamiltonian

$$H = - \sum_{ij\sigma} t_{ij} (\hat{c}_{i\sigma}^\dagger \hat{c}_{j\sigma} + h.c.) + U \sum_i \hat{n}_{i\uparrow} \hat{n}_{i\downarrow}. \quad (1)$$

This is one of the simplest models that respect the orthorhombic symmetry in real materials. Here $\hat{c}_{i\sigma}^\dagger$ ($\hat{c}_{i\sigma}$) is the electron creation (annihilation) operator on-site $i = (x_i, y_i)$ with spin- σ , and $\hat{n}_{i\sigma}$ is the electron number operator. The electron hopping amplitude $t_{ij} = t$ if i and j are nearest neighbors and $t_{ij} = t'(1 \pm \Delta_{t'})$ for next-nearest neighbors where $\Delta_{t'}$ is the spatial anisotropy related to the orthorhombic distortion as shown in Fig. 5a. U is the on-site Coulomb repulsion. We set $t = 1$ as an energy unit with interaction $U = 12t$ and report results for $t' = -0.3t \sim -0.1t$, which corresponds to the typical values reported in the literature for LSCO⁴²⁻⁴⁴ with doping near $\delta = 12.5\%$, the hole concentration used in our study. The main results are shown in Figs. 5, 6 and the details are given below. Additional details can be found in Supplementary Note 4 and Supplementary Figs. 10–20.

We first calculate the electron density distribution $n(x, y) = \langle \hat{n}(x, y) \rangle$, where an example is shown in Fig. 5b for $t' = -0.2t$ and $\Delta_{t'} = 0.4$. In the absence of spatial anisotropy, i.e., $\Delta_{t'} = 0$, we find the charge stripe (parallel to the y direction) of wavelength $\lambda_c \approx 4$ (see Supplementary Fig. 10a), consistent with the half-filled charge stripes observed in previous studies^{18,19,21,22}. In our simulations, the charge stripe being bond-centered is due to the even number of sites along the x direction in the calculation. Our results show that the charge stripe is tilted when $\Delta_{t'} > 0$ as shown in Fig. 5b–d, consistent with the experimental observations. This tilting reduces the kinetic energy of the charge stripe^{45,46}. To support this, we further calculate the kinetic energy for both $t'(1 \pm \Delta_{t'})$ bonds as $E_k(\pm \Delta_{t'}) = -t'(1 \pm \Delta_{t'}) \sum_{ij \in (1 \pm \Delta_{t'})\text{-bonds}} \langle \hat{c}_{i\sigma}^\dagger \hat{c}_{j\sigma} \rangle$. The kinetic energy difference $dE_k(\pm \Delta_{t'}) = E_k(\pm \Delta_{t'}) - E_k(\Delta_{t'} = 0)$ is shown in Fig. 5e. While the kinetic energy along the $(1 - \Delta_{t'})$ -bonds is increased, i.e., $dE_k(-\Delta_{t'}) > 0$, the kinetic energy along the $(1 + \Delta_{t'})$ -bonds is reduced, so that the total kinetic energy $dE_k = dE_k(\Delta_{t'}) + dE_k(-\Delta_{t'}) < 0$ when $\Delta_{t'} > 0$. We note that a finite value of $\Delta_{t'} > 0.1$ is necessary to give observable tilting of the stripes due to limited sample size along y direction in the calculations, although the eight-leg ladder size in DMRG calculations with the presented accuracy is already unprecedented as far as we are aware.

To describe the magnetic properties of the system, we have also calculated the static spin structure factor, which is defined as

$$S(\mathbf{Q}) = \frac{1}{N} \sum_{ij=1}^N e^{ik \cdot (\mathbf{r}_i - \mathbf{r}_j)} \langle \mathbf{S}_i \cdot \mathbf{S}_j \rangle. \quad (2)$$

Here the wavevector $\mathbf{Q} = (k_x, k_y) = k_x \mathbf{b}_x + k_y \mathbf{b}_y$ in reciprocal space is defined by the reciprocal vectors $\mathbf{b}_x = (2\pi, 0)$ and $\mathbf{b}_y = (0, 2\pi)$. Consistent with previous studies^{18,19,21,22}, we find that the spin-spin correlations show a spatial oscillation of wavelength λ_s that is mutually commensurate with the CDW order, i.e., $\lambda_s \approx 2\lambda_c$. As a result, $S(\mathbf{Q})$ is peaked at the momentum (k_x, k_y) where $k_x = 0.5 \pm 0.125$ and $k_y = 0.5$. Similar with the charge stripe, we find that the peak position of $S(\mathbf{Q})$ is shifted with $\Delta_{t'}$ as shown in Fig. 5f and g. The peak shift, i.e., the difference of peak positions along y direction for this pair of peaks in $S(\mathbf{Q})$, and its dependence on $\Delta_{t'}$ is given in Fig. 6. We focus on $t' = -0.2t$, and find that the relationship between the peak shift and $\Delta_{t'}$ can be well fitted by a quadratic function, which is commonly used in the analysis of DMRG data^{21,26}. The use of the quadratic function passing origin without a threshold value in $\Delta_{t'}$ is also consistent with the previous phenomenological study¹⁷, which showed that the tilting is proportional to the orthorhombicity to first order approximation.

Comparing our results with experimental observation allows us to estimate the spatial anisotropy of t' in the real material. If we interpolate the above empirical curve to the experimental observed value of the peak shift in our LSCO sample, the expected anisotropy is $\Delta_{t'} = 2.3(1)\%$. This estimation of $\Delta_{t'}$ depends somewhat on the value of t' . For $t' = -0.3t \sim -0.1t$, if we assume the peak shift follows the same quadratic form, the estimated $\Delta_{t'}$ can vary between 1.8%–3.6%, which is pretty close to the prediction ($\Delta_{t'} \gtrsim 1.5\%$) from previous studies^{47,48}. Note that $\Delta_{t'}$ has not been determined experimentally yet, even with advanced spectroscopic techniques such as angle-resolved photoemission spectroscopy (ARPES). This could be due to its small effect on the band structure. Additionally, the presence of the structural twinning may further obscure the interpretation of such measurements.

We can estimate the energy scale of the tilted stripes. The difference between the hopping integral for the two diagonal directions is $|2t'\Delta_{t'}|$. Taking $\Delta_{t'} = 0.023$, $t' = -0.2t$, and $t = 0.43 \text{ eV}$ ^{42,49}, we have $|2t'\Delta_{t'}| = 4.0 \text{ meV} \sim 46 \text{ K}$. This is consistent with the temperature range where the Y -shift can be clearly detected with neutron scattering. At higher temperatures, thermal broadening may obscure the small shift of the peak positions.

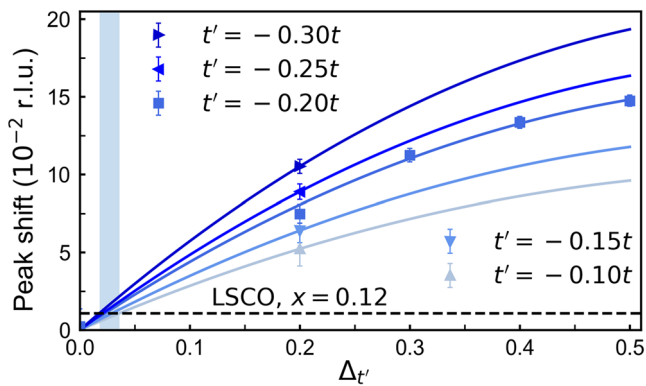


Fig. 6 | The spin stripe tilting as a function of $\Delta t'$ for different t' . The tilting is measured by the peak shift along K direction between the pair of peaks in $S(\mathbf{Q})$ maps (shown in Fig. 5f and Supplementary Figs. 11 and 14). The solid line for $t' = -0.2t$ is a quadratic fit to the data. Other lines are the same quadratic curve as for $t' = -0.2t$ but scaled to match the corresponding data. The horizontal dashed line indicates the elastic peak shift measured in our LSCO sample. The vertical bar represents the range of our estimated $\Delta t'$, determined by the intersection of the fitted curves and the dashed line. Error bars correspond to $\pm\sigma$, where σ is the standard deviation.

The above calculations are performed on a system size of $N = 16 \times 8$, where $L_x = 16$ and $L_y = 8$ are the number of sites in \hat{x} and \hat{y} directions, respectively. The reason that we use eight-leg ladder system size is because this appears to be the minimal size required to produce half-filled stripes with ordinary d -wave symmetry compatible with experimental observations. For comparison, the ground state superconducting pairing symmetry is the plaquette d -wave on the hole doped side ($t' < 0$) for the four-leg ladder system³³, while half-filled charge stripes are forbidden for the six-leg ladder system if superconducting Cooper pairs are present⁵⁰. To show that the boundary effects and finite-size effects have negligible impacts on our fitted peak shifts, we performed more numerical calculations with different system sizes ($N = 12 \times 8$ and $N = 8 \times 8$). The results indeed show good convergence between $N = 12 \times 8$ and $N = 16 \times 8$ system sizes, supporting the accuracy of our calculations. More details can be found in Supplementary Figs. 17–20. We note that our results are based on local charge and spin modulations instead of the long-range decaying behavior of the correlation functions and therefore should not be affected by the exact nature of the ground state being stripes or d -wave superconductivity in the model.

Discussion

The primary conclusions from our combined experimental and numerical work can be summarized in three main points: (1) two types of phases coexist in our sample—a minority phase with static SDW and a majority phase with fluctuating spin stripes, (2) both phases have tilted stripes (Y -shift) with the same degree of tilting, and (3) the origin of the tilting can be explained by a small anisotropy in the hopping interaction t' . We elaborate on the implications of these results below.

Our elastic and inelastic neutron scattering results are naturally explained by the presence of two distinct phases (one with static spin stripes and one with fluctuating spin stripes). As discussed in the elastic scattering results, we estimate that only a small fraction (~5%) of the sample is magnetically ordered. The observation of a partially magnetically ordered phase in LSCO has been previously reported by μ SR studies^{39,51}. This is further supported by recent x-ray scattering studies that two types of CDW orders coexist in LSCO, where the longer-range ordered CDW takes place in a minority fraction of the sample^{15,16}. This suggests that the phase with static SDW has a type of CDW order which is distinguished by having longer-range correlations.

The low symmetry of the Y -shift positions combined with high-resolution measurements enabled us to determine the spin direction and interlayer correlations. So far as we know, this is the first time that the spin direction is explicitly determined to be along the orthorhombic \mathbf{b}_0 direction

in LSCO. The rather short interlayer correlation length of $\sim 7 \text{ \AA}$ is consistent with the previous reports in both SDW and CDW studies in LSCO^{12,52–54}, affirming the 2D nature of the stripe order. Such short interlayer correlations could be explained by stacking faults between layers (see Supplementary Fig. 4). The spin direction and local interlayer correlations are similar to those in the parent compound La_2CuO_4 . This reiterates that doped antiferromagnets are essential to the description of high- T_c cuprates⁵⁵.

The inelastic scattering measurements of the isotropic nature of the spin fluctuations requires the presence of an additional phase. Since spin-wave excitations can only contain transverse fluctuations below T_{sdw} , the measured isotropic excitations indicates that there is a majority phase that is not magnetically ordered, characterized with isotropic spin excitations. In contrast, the minority phase with static SDW order should have only transverse spin excitations. Therefore, the peak shift in Fig. 3c represents the average of the isotropic and transverse contributions, weighted by their respective volume fractions, which is dominated by the non-magnetically ordered phase. This majority phase should also be responsible for the superconductivity in the sample, which is a bulk superconductor. The minority phase may not be superconducting due to competition with the static SDW.

As discussed in the inelastic scattering results, the intensities and widths of the fluctuating spin stripe peaks has a close correlation to the CDW peaks observed with x-rays. These intimate relationships suggest that the two signals detected by different tools probably originate from the same majority phase. This is consistent with the recent NMR finding that increasing charge ordered domains trigger the glassy freezing of Cu spins below T_{cdw} ⁵⁶.

We find that both phases contain tilted stripe correlations with the same tilt angle of $\sim 3.0^\circ$. Our data and analysis indicate that the same Y -shift is an intrinsic property of both static and fluctuation phases. This contrasts with a previous study of oxygen-doped LCO where it was concluded that the spin fluctuations have a significantly different stripe tilt angle compared to the static SDW order¹⁴. Our numerical results which explain the Y -shift indicate that the static and fluctuating stripes should have the same tilting, as it depends only on the underlying orthorhombicity.

DMRG calculations provide a direct and unbiased way to understand the origin of the Y -shift phenomenon. The parameters in our state-of-the-art calculations on eight-leg ladders are consistent with the structure of real materials. The anisotropy of t' may arise from inequivalent CuO_6 octahedron tilts and unequal lattice parameters between the orthorhombic a_0 and b_0 axes. Here, it is estimated to be $\gtrsim 1.5\%$ in LSCO with $x = 0.12$ ^{47,48}. Our DMRG prediction for the anisotropy $\Delta t' = 1.8\% \sim 3.6\%$ matches this expected value for LSCO very well, and much better than the mean field approach based on Fermi surface nesting^{47,48}. Moreover, our results reveal the importance of kinetic energy considerations in stripe formation⁵⁷. Microscopically, the anisotropy of t' causes the stripes to tilt towards the short \mathbf{a}_0 axis, the direction with larger hopping magnitude and gain in kinetic energy. This is an obvious manifestation of the role of kinetic energy term in stabilizing charge stripes by having delocalized holes along the stripes^{45,58}. Our DMRG results also qualitatively agree with an early exact diagonalization study⁵⁹, which found that an anisotropic t' in the extended t - J model results in a preferred orientation of stripes formed by doped holes.

The explanatory power of our results can further be tested by their applicability to similar orthorhombic cuprate materials. Indeed, the Y -shift has been reported in both CDW and SDW orders with various dopants in La-based cuprates^{7–12,15,16}. Tilted SDW order was also found in LSCO at lower doping level of $x = 0.07$ ¹³, with a surprisingly large tilt angle. In the above cases, the larger tilt angle goes hand-in-hand with a larger structural orthorhombicity, as expected in our explanation based on anisotropic t' . A different class of stripes (i.e., diagonal stripes) have been observed in lightly-doped LSCO^{60–62} and $\text{La}_{2-x}\text{Ba}_x\text{CuO}_4$ (LBCO)⁶³ below $x \sim 0.055$, coincident with a superconductor-to-insulator transition. Since these diagonal stripes are aligned along the shorter \mathbf{a}_0 direction, this could be regarded as the extreme case of our tilted stripe explanation. Such unidirectional diagonal stripes are not limited to cuprates—they were also found in the insulating

nickelates⁶⁴, implying the possible generality of this mechanism for the selection of the stripe direction in systems with similar orthorhombic symmetry.

Uniaxial strain engineering offers a powerful tuning knob to artificially modify the hopping strengths along specific directions. We note that a recent x-ray scattering study⁶⁵ observed a decrease in stripe tilt angle in LSCO under uniaxial pressure applied along one of the tetragonal directions. This agrees with our kinetic energy argument that the stripe direction should be sensitive to the anisotropy of the hopping terms. Such uniaxial pressure can result in an anisotropy in t . In another recent elastic neutron scattering experiment⁶⁶, uniaxial pressure was used to select a single magnetic domain in LSCO with the stripe direction aligning along the larger t direction. LSCO has intrinsic anisotropy in t due to octahedron rotation along the Cu-Cu bond directions. A recent uniaxial strain experiment in LSCO reports surprisingly different behaviors in elastic and inelastic channels in terms of incommensurability⁶⁷. In the future, it would be appealing to investigate numerically how the tilt angle would change with both anisotropic t and t' terms in the Hamiltonian.

These results show an excellent match between DMRG calculations for the doped Hubbard model and the specific ground state details observed in $\text{La}_{1.88}\text{Sr}_{0.12}\text{CuO}_4$ —attesting to the appropriateness of the model for the cuprates. Our results further stress the importance of t' in the Hamiltonian. The presence of t' is known to stabilize half-filled stripes and superconductivity, which are both present in our LSCO sample^{19,21,22}. The specific alignment direction of the stripes is so sensitive to t' where even a small anisotropy in t' can result in the subtle observed tilting. This highlights how the phases of stripes and superconductivity are sensitively intertwined at the level of model calculations and accounts for the appearance of these phases in a real material. Of course, the phenomenology of density wave ordering is different in LSCO compared to YBCO. This calls for a better understanding of how small changes in the Hamiltonian parameters, perhaps arising from subtle structural differences, can account for variations in the competing states across the families of cuprate materials.

Methods

Sample details

The single crystal of LSCO with a nominal doping of $x = 0.12$ was grown by the traveling-solvent-floating-zone method. As-grown crystal was annealed in oxygen gas flow at 900 °C for 72 h. At room temperature, the lattice constants are $a = b = 3.780$ Å and $c = 13.218$ Å determined by powder x-ray diffraction on a crushed piece of the single crystal. The structural transition temperature from the high-temperature tetragonal phase to the low-temperature orthorhombic phase is $T_s = 242$ K determined by extinction of the nuclear Bragg peak (2, 0, 0) in neutron diffraction measurements upon warming. Both the lattice constants and the structural transition temperature T_s agree pretty well with the previous reported results from powder and single crystal samples^{8,32,68}, reassuring the Sr content. To avoid the large mosaic that could be introduced from the coalignment of multiple samples, only one large single crystal with a mass of 12.8 g was used in our neutron scattering experiments. The size of the crystal is 8 mm ϕ × 40 mm.

Neutron measurements

The neutron experiments were carried out at the thermal-neutron beamline HB-1A at the high flux isotope reactor (HFIR) at Oak Ridge National Laboratory and the cold-neutron beamline at the Spin Polarized Inelastic Neutron Spectrometer (SPINS) at the Center for Neutron Research (NCNR) at the National Institute of Standards and Technology (NIST). For HB-1A, the incident energy was fixed at 14.65 meV with horizontal collimations of 40'–40'–sample–40'–80'. For SPINS, the final energy was fixed at 5 meV, and most of measurements were done with horizontal collimations of guide–open–sample–80'–open, except for the mesh-scan near nuclear Bragg peak (1, 1, 0) (see Supplementary Fig. 1), which was with tighter horizontal collimations of guide–20'–sample–20'–open. The sample was mounted on an aluminum holder and aligned in the ($HK0$) plane. Base temperatures of $T = 5$ K (HB-1A) and $T = 2.8$ K (SPINS) were achieved

using closed-cycle refrigerators. The sample was cooled slowly with a rate of ~ 2 K per minute from room temperature.

Both the elastic scattering (Fig. 1) and temperature dependence of the inelastic scattering near (0.5, 0.5, 0) (Fig. 4) were measured at HB-1A. The elastic scattering near (1, 1, 0) (Supplementary Fig. 1) and (0.5, 1.5, 0) (Fig. 2) and energy dependence of the inelastic scattering near (0.5, 0.5, 0) (Fig. 3) were measured at SPINS. We note that the sample was rotated by 90° in-plane between the HB-1A and SPINS experiments, so the same structural domains between the two experiments were related by this 90° rotation. For example, the green domain measured at SPINS corresponds to the red one at HB-1A. This has been taken into account in the analysis of HB-1A data when domain population information is needed (including Supplementary Fig. 2 and the moment size calculation).

Numerical calculations

We employed the DMRG³³ method to study the ground state properties of the t - t' Hubbard model as defined in Eq. (1). We considered the square lattice with open boundary conditions in both directions specified by the basis vectors $\hat{x} = (1, 0)$ and $\hat{y} = (0, 1)$. The total number of sites is $N = 16 \times 8$, where $L_x = 16$ and $L_y = 8$ are the number of sites in \hat{x} and \hat{y} directions, respectively. The doped hole concentration is defined as $\delta = (N - N_e)/N$ with N_e the number of electrons. Additional calculations were performed with smaller sample sizes ($N = 12 \times 8$ and $N = 8 \times 8$) at the same hole concentration. We performed around 60 sweeps in the current DMRG simulation and kept up to $m = 25,000$ number of states with a typical truncation error $\epsilon \approx 2 \times 10^{-5}$.

Data availability

All data needed to evaluate the findings in this paper are present in the paper and/or the Supplementary Information, and are available from the corresponding authors upon reasonable request.

Code availability

The codes implementing the calculations of this study are available from the corresponding authors upon reasonable request.

Received: 12 March 2024; Accepted: 18 July 2024;

Published online: 31 July 2024

References

1. Fradkin, E., Kivelson, S. A. & Tranquada, J. M. Colloquium: theory of intertwined orders in high temperature superconductors. *Rev. Mod. Phys.* **87**, 457–482 (2015).
2. Keimer, B., Kivelson, S. A., Norman, M. R., Uchida, S. & Zaanen, J. From quantum matter to high-temperature superconductivity in copper oxides. *Nature* **518**, 179–186 (2015).
3. Comin, R. & Damascelli, A. Resonant x-ray scattering studies of charge order in cuprates. *Annu. Rev. Condens. Matter Phys.* **7**, 369–405 (2016).
4. Tranquada, J. M., Sternlieb, B. J., Axe, J. D., Nakamura, Y. & Uchida, S. Evidence for stripe correlations of spins and holes in copper oxide superconductors. *Nature* **375**, 561–563 (1995).
5. Tranquada, J. M. Spins, stripes, and superconductivity in hole-doped cuprates. *AIP Conf. Proc.* **1550**, 114–187 (2013).
6. Tranquada, J. M. Cuprate superconductors as viewed through a striped lens. *Adv. Phys.* **69**, 437–509 (2020).
7. Lee, Y. S. Neutron-scattering study of spin-density wave order in the superconducting state of excess-oxygen-doped $\text{La}_2\text{CuO}_{4+y}$. *Phys. Rev. B* **60**, 3643–3654 (1999).
8. Kimura, H. Incommensurate geometry of the elastic magnetic peaks in superconducting $\text{La}_{1.88}\text{Sr}_{0.12}\text{CuO}_4$. *Phys. Rev. B* **61**, 14366–14369 (2000).
9. Matsushita, H. Sr concentration dependence of incommensurate elastic magnetic peaks in $\text{La}_{2-x}\text{Sr}_x\text{CuO}_4$. *J. Phys. Chem. Solids* **60**, 1071–1074 (1999).

10. Fujita, M., Goka, H., Yamada, K. & Matsuda, M. Structural effect on the static spin and charge correlations in $\text{La}_{1.875}\text{Ba}_{0.125-x}\text{Sr}_x\text{CuO}_4$. *Phys. Rev. B* **66**, 184503 (2002).
11. Thampy, V. Rotated stripe order and its competition with superconductivity in $\text{La}_{1.88}\text{Sr}_{0.12}\text{CuO}_4$. *Phys. Rev. B* **90**, 100510 (2014).
12. Rømer, A. T. Field-induced interplanar magnetic correlations in the high-temperature superconductor $\text{La}_{1.88}\text{Sr}_{0.12}\text{CuO}_4$. *Phys. Rev. B* **91**, 174507 (2015).
13. Jacobsen, H. Neutron scattering study of spin ordering and stripe pinning in superconducting $\text{La}_{1.93}\text{Sr}_{0.07}\text{CuO}_4$. *Phys. Rev. B* **92**, 174525 (2015).
14. Jacobsen, H. Distinct nature of static and dynamic magnetic stripes in cuprate superconductors. *Phys. Rev. Lett.* **120**, 037003 (2018).
15. Wen, J.-J. Observation of two types of charge-density-wave orders in superconducting $\text{La}_{2-x}\text{Sr}_x\text{CuO}_4$. *Nat. Commun.* **10**, 3269 (2019).
16. Wen, J.-J. Enhanced charge density wave with mobile superconducting vortices in $\text{La}_{1.885}\text{Sr}_{0.115}\text{CuO}_4$. *Nat. Commun.* **14**, 733 (2023).
17. Robertson, J. A., Kivelson, S. A., Fradkin, E., Fang, A. C. & Kapitulnik, A. Distinguishing patterns of charge order: stripes or checkerboards. *Phys. Rev. B* **74**, 134507 (2006).
18. White, S. R. & Scalapino, D. J. Density matrix renormalization group study of the striped phase in the $2d\ t - J$ model. *Phys. Rev. Lett.* **80**, 1272–1275 (1998).
19. White, S. R. & Scalapino, D. J. Competition between stripes and pairing in a $t-t'-J$ model. *Phys. Rev. B* **60**, R753–R756 (1999).
20. Machida, K. & Ichioka, M. Stripe structure, spectral feature and soliton gap in High T_c cuprates. *J. Phys. Soc. Jpn.* **68**, 2168–2171 (1999).
21. Jiang, H.-C. & Devereaux, T. P. Superconductivity in the doped Hubbard model and its interplay with next-nearest hopping t' . *Science* **365**, 1424–1428 (2019).
22. Jiang, Y.-F., Zaanen, J., Devereaux, T. P. & Jiang, H.-C. Ground state phase diagram of the doped Hubbard model on the four-leg cylinder. *Phys. Rev. Res.* **2**, 033073 (2020).
23. Chung, C.-M., Qin, M., Zhang, S., Schollwöck, U. & White, S. R. Plaquette versus ordinary d -wave pairing in the t' -Hubbard model on a width-4 cylinder. *Phys. Rev. B* **102**, 041106 (2020).
24. Lu, X., Chen, F., Zhu, W., Sheng, D. N. & Gong, S.-S. Emergent superconductivity and competing charge orders in hole-doped square-lattice $t-J$ model. *Phys. Rev. Lett.* **132**, 066002 (2024).
25. Xu, H. Coexistence of superconductivity with partially filled stripes in the Hubbard model. *Science* **384**, eadh7691 (2024).
26. Qin, M. Absence of superconductivity in the pure two-dimensional hubbard model. *Phys. Rev. X* **10**, 031016 (2020).
27. Batista, C. D., Ortiz, G. & Balatsky, A. V. Unified description of the resonance peak and incommensuration in high- T_c superconductors. *Phys. Rev. B* **64**, 172508 (2001).
28. Kivelson, S. A. How to detect fluctuating stripes in the high-temperature superconductors. *Rev. Mod. Phys.* **75**, 1201–1241 (2003).
29. Vojta, M., Vojta, T. & Kaul, R. K. Spin excitations in fluctuating stripe phases of doped cuprate superconductors. *Phys. Rev. Lett.* **97**, 097001 (2006).
30. Huang, E. W. Numerical evidence of fluctuating stripes in the normal state of high- T_c cuprate superconductors. *Science* **358**, 1161–1164 (2017).
31. Vojta, M. Lattice symmetry breaking in cuprate superconductors: stripes, nematics, and superconductivity. *Adv. Phys.* **58**, 699–820 (2009).
32. Yamada, K. Doping dependence of the spatially modulated dynamical spin correlations and the superconducting-transition temperature in $\text{La}_{2-x}\text{Sr}_x\text{CuO}_4$. *Phys. Rev. B* **57**, 6165–6172 (1998).
33. White, S. R. Density matrix formulation for quantum renormalization groups. *Phys. Rev. Lett.* **69**, 2863–2866 (1992).
34. Braden, M. Characterization and structural analysis of twinned $\text{La}_{2-x}\text{Sr}_x\text{CuO}_{4\pm\delta}$ crystals by neutron diffraction. *Phys. C: Supercond.* **191**, 455–468 (1992).
35. Vaknin, D. Antiferromagnetism in $\text{La}_2\text{CuO}_{4-y}$. *Phys. Rev. Lett.* **58**, 2802–2805 (1987).
36. Warren, B. X-ray diffraction (Dover Publications, 1990).
37. Kimura, H. Neutron-scattering study of static antiferromagnetic correlations in $\text{La}_{2-x}\text{Sr}_x\text{Cu}_{1-y}\text{Zn}_y\text{O}_4$. *Phys. Rev. B* **59**, 6517–6523 (1999).
38. Kimura, H. Neutron scattering study of incommensurate elastic magnetic peaks in $\text{La}_{1.88}\text{Sr}_{0.12}\text{CuO}_4$. *J. Phys. Chem. Solids* **60**, 1067–1070 (1999).
39. Savici, A. T. Muon spin relaxation studies of incommensurate magnetism and superconductivity in stage-4 $\text{La}_2\text{CuO}_{4.11}$ and $\text{La}_{1.88}\text{Sr}_{0.12}\text{CuO}_4$. *Phys. Rev. B* **66**, 014524 (2002).
40. Tuțeanu, A.-E. Nature of the magnetic stripes in fully oxygenated $\text{La}_2\text{CuO}_{4+y}$. *Phys. Rev. B* **103**, 045138 (2021).
41. Kofu, M. Hidden quantum spin-gap state in the static stripe phase of high-temperature $\text{La}_{2-x}\text{Sr}_x\text{CuO}_4$ superconductors. *Phys. Rev. Lett.* **102**, 047001 (2009).
42. Pavarini, E., Dasgupta, I., Saha-Dasgupta, T., Jepsen, O. & Andersen, O. K. Band-structure trend in hole-doped cuprates and correlation with $T_{c\text{max}}$. *Phys. Rev. Lett.* **87**, 047003 (2001).
43. Damascelli, A., Hussain, Z. & Shen, Z.-X. Angle-resolved photoemission studies of the cuprate superconductors. *Rev. Mod. Phys.* **75**, 473–541 (2003).
44. Peng, Y. Y. Influence of apical oxygen on the extent of in-plane exchange interaction in cuprate superconductors. *Nat. Phys.* **13**, 1201–1206 (2017).
45. Zaanen, J. & Gunnarsson, O. Charged magnetic domain lines and the magnetism of high- T_c oxides. *Phys. Rev. B* **40**, 7391–7394 (1989).
46. Kato, M., Machida, K., Nakanishi, H. & Fujita, M. Soliton lattice modulation of incommensurate spin density wave in two dimensional hubbard model – a mean field study-. *J. Phys. Soc. Jpn.* **59**, 1047–1058 (1990).
47. Yamase, H. & Kohno, H. Possible quasi-one-dimensional fermi surface in $\text{La}_{2-x}\text{Sr}_x\text{CuO}_4$. *J. Phys. Soc. Jpn.* **69**, 332–335 (2000).
48. Yamase, H. & Kohno, H. Shift of incommensurate antiferromagnetic peaks in $\text{La}_{2-x}\text{Sr}_x\text{CuO}_4$. *Phys. Rev. B* **68**, 014502 (2003).
49. Hybertsen, M. S., Stechel, E. B., Schluter, M. & Jennison, D. R. Renormalization from density-functional theory to strong-coupling models for electronic states in Cu-O materials. *Phys. Rev. B* **41**, 11068–11072 (1990).
50. Jiang, Y.-F., Devereaux, T. P. & Jiang, H.-C. Ground-state phase diagram and superconductivity of the doped hubbard model on six-leg square cylinders. *Phys. Rev. B* **109**, 085121 (2024).
51. Chang, J. Tuning competing orders in $\text{La}_{2-x}\text{Sr}_x\text{CuO}_4$ cuprate superconductors by the application of an external magnetic field. *Phys. Rev. B* **78**, 104525 (2008).
52. Lake, B. Three-dimensionality of field-induced magnetism in a high-temperature superconductor. *Nat. Mater.* **4**, 658–662 (2005).
53. Croft, T. P., Lester, C., Senn, M. S., Bombardi, A. & Hayden, S. M. Charge density wave fluctuations in $\text{La}_{2-x}\text{Sr}_x\text{CuO}_4$ and their competition with superconductivity. *Phys. Rev. B* **89**, 224513 (2014).
54. Christensen, N. B. et al. Bulk charge stripe order competing with superconductivity in $\text{La}_{2-x}\text{Sr}_x\text{CuO}_4$ ($x=0.12$). <https://arxiv.org/abs/1404.3192> (2014).
55. Orenstein, J. & Millis, A. J. Advances in the physics of high-temperature superconductivity. *Science* **288**, 468–474 (2000).
56. Arsenault, A., Imai, T., Singer, P. M., Suzuki, K. M. & Fujita, M. Magnetic inhomogeneity in charge-ordered $\text{La}_{1.885}\text{Sr}_{0.115}\text{CuO}_4$ studied by NMR. *Phys. Rev. B* **101**, 184505 (2020).
57. Zachar, O., Kivelson, S. A. & Emery, V. J. Landau theory of stripe phases in cuprates and nickelates. *Phys. Rev. B* **57**, 1422–1426 (1998).

58. Emery, V. J., Kivelson, S. A. & Tranquada, J. M. Stripe phases in high-temperature superconductors. *Proc. Nat. Acad. Sci. USA* **96**, 8814–8817 (1999).
59. Tipper, J. M. & Vos, K. J. E. Formation of stripes and incommensurate peaks in the orthorhombic phase of underdoped $\text{La}_{2-x}\text{Sr}_x\text{CuO}_4$. *Phys. Rev. B* **67**, 144511 (2003).
60. Wakimoto, S. Observation of incommensurate magnetic correlations at the lower critical concentration for superconductivity in $\text{La}_{2-x}\text{Sr}_x\text{CuO}_4$ ($x=0.05$). *Phys. Rev. B* **60**, R769–R772 (1999).
61. Fujita, M. Static magnetic correlations near the insulating-superconducting phase boundary in $\text{La}_{2-x}\text{Sr}_x\text{CuO}_4$. *Phys. Rev. B* **65**, 064505 (2002).
62. Matsuda, M. Electronic phase separation in lightly doped $\text{La}_{2-x}\text{Sr}_x\text{CuO}_4$. *Phys. Rev. B* **65**, 134515 (2002).
63. Dunsiger, S. R. Diagonal and collinear incommensurate spin structures in underdoped $\text{La}_{2-x}\text{Ba}_x\text{CuO}_4$. *Phys. Rev. B* **78**, 092507 (2008).
64. Hücker, M. Unidirectional diagonal order and three-dimensional stacking of charge stripes in orthorhombic $\text{Pr}_{1.67}\text{Sr}_{0.33}\text{NiO}_4$ and $\text{Nd}_{1.67}\text{Sr}_{0.33}\text{NiO}_4$. *Phys. Rev. B* **74**, 085112 (2006).
65. Wang, Q. Uniaxial pressure induced stripe order rotation in $\text{La}_{1.88}\text{Sr}_{0.12}\text{CuO}_4$. *Nat. Commun.* **13**, 1795 (2022).
66. Simutis, G. Single-domain stripe order in a high-temperature superconductor. *Commun. Phys.* **5**, 296 (2022).
67. Kamminga, M. E. Evolution of magnetic stripes under uniaxial stress in $\text{La}_{1.885}\text{Ba}_{0.115}\text{CuO}_4$ studied by neutron scattering. *Phys. Rev. B* **107**, 144506 (2023).
68. Radaelli, P. G. Structural and superconducting properties of $\text{La}_{2-x}\text{Sr}_x\text{CuO}_4$ as a function of Sr content. *Phys. Rev. B* **49**, 4163–4175 (1994).
69. Hunter, J. D. Matplotlib: a 2D graphics environment. *Comput. Sci. Eng.* **9**, 90–95 (2007).

Acknowledgements

This work was supported by the U.S. Department of Energy, Office of Science, Basic Energy Sciences, Materials Sciences, and Engineering Division, under contract DE-AC02-76SF00515. Research conducted at ORNL's High Flux Isotope Reactor was sponsored by the Scientific User Facilities Division, Office of Basic Energy Sciences, US Department of Energy. We acknowledge the support of the National Institute of Standards and Technology, U.S. Department of Commerce, in providing the neutron research facilities used in this work. M.F. was supported by Grant-in-Aid for Scientific Research (A) (Grant Nos. 16H02125 and 21H04448).

Author contributions

The project was conceived by Y.S.L. W.H., J.W., G.X., and W.T. performed the neutron scattering measurements, and W.H. analyzed the data. T.T., Y.I., and M.F. synthesized the sample. H.C.J. performed the numerical calculations. The paper was written by W.H., H.C.J., and Y.S.L. with input from all co-authors.

Competing interests

The authors declare no competing interests.

Additional information

Supplementary information The online version contains supplementary material available at <https://doi.org/10.1038/s42005-024-01753-z>.

Correspondence and requests for materials should be addressed to Wei He or Young S. Lee.

Peer review information *Communications Physics* thanks Shou-Shu Gong and the other, anonymous, reviewer(s) for their contribution to the peer review of this work. A peer review file is available.

Reprints and permissions information is available at <http://www.nature.com/reprints>

Publisher's note Springer Nature remains neutral with regard to jurisdictional claims in published maps and institutional affiliations.

Open Access This article is licensed under a Creative Commons Attribution 4.0 International License, which permits use, sharing, adaptation, distribution and reproduction in any medium or format, as long as you give appropriate credit to the original author(s) and the source, provide a link to the Creative Commons licence, and indicate if changes were made. The images or other third party material in this article are included in the article's Creative Commons licence, unless indicated otherwise in a credit line to the material. If material is not included in the article's Creative Commons licence and your intended use is not permitted by statutory regulation or exceeds the permitted use, you will need to obtain permission directly from the copyright holder. To view a copy of this licence, visit <http://creativecommons.org/licenses/by/4.0/>.

© The Author(s) 2024